ACTA IMEKO
ISSN: 2221-870X
September 2026, Volume 15, Number 3, 1 – 7

X-ray computed tomography for non-destructive evaluation of steel wire ropes: Comparison of laboratory XCT configurations for image quality and damage visualization

Daniel Kytyr[1], Petr Koudelka[1], Jan Sleichrt[1], Jaroslav Kylar[2], Radka Hrazdirova[3], Jiri Lahodny[3]

[1] *Czech Academy of Sciences, Institute of Theoretical and Applied Mechanics, Prague, Czechia*
[2] *Czech Technical University in Prague, Faculty of Transportation Sciences, Prague, Czechia*
[3] *EXCON, a. s., Prague, Czechia*

ABSTRACT
Steel wire ropes are critical structural components whose internal damage often cannot be reliably assessed using conventional non-destructive testing methods. This study evaluates the applicability of laboratory X-ray computed microtomography (XCT) for detailed inspection of steel wire ropes by comparing three complementary XCT configurations: one employing a liquid-metal anode microfocus source with a large-area flat-panel detector, a conventional sealed-type microfocus tube with CMOS detector, and a high-power X-ray source coupled with scintillating screen and a laboratory camera. Intact and damaged rope specimens together with an individual fractured steel wire were investigated under various acquisition conditions. Image quality was quantitatively assessed using the contrast-to-noise ratio (CNR) and the full width at half maximum (FWHM) of the line spread function, complemented by qualitative evaluation of reconstructed three-dimensional models. The results demonstrate the influence of X-ray source characteristics and the acquisition parameters on image quality and defect detectability. Although the high-power system provided superior penetration capability and the highest CNR, its large focal point substantially limited the achievable spatial resolution. In contrast, both microfocus configurations enabled reliable visualization of individual wires and internal damage features, with image quality strongly dependent on the number of acquired projections. The presented comparison provides practical guidance for selecting appropriate laboratory XCT configurations for non-destructive evaluation of steel wire ropes and similar highly attenuating engineering components.

Section: RESEARCH PAPER

Keywords: steel wire ropes; non-destructive testing; X-ray computed tomography; image quality assessment; contrast-to-noise ratio; spatial resolution

Citation: D. Kytyr, P. Koudelka, J. Sleichrt, J. Kylar, R. Hrazdirova, J. Lahodny, X-ray computed tomography for non-destructive evaluation of steel wire ropes: Comparison of laboratory XCT configurations for image quality and damage visualization, Acta IMEKO, vol. 15 (2026) no. 3, pp. 1–7. DOI: 10.21014/actaimeko.v15i3.2456

Section Editor: Emina Hadzalic, University of Rijeka, Croatia

Received: July 2, 2026; **In Final Form:** August 19, 2026; **Published:** September, 2026.

Copyright: This is an open-access article distributed under the terms of the Creative Commons Attribution 4.0 International License.

Funding: The research was supported by the European Union under the INODIN project no. CZ.02.01.01/00/23_020/0008487.

Corresponding Author: Daniel Kytyr, e-mail: kytyr@itam.cas.cz

1. INTRODUCTION

Steel wire ropes are critical load-bearing components that are used in lifting systems, cable-supported bridges, offshore structures, and transportation infrastructure. Their structural integrity is directly affected by defects such as wire fractures, corrosion, wear, or local loss of the metallic cross-sectional area. Due to their multi-strand architecture, damage may develop within the rope core and remain inaccessible to direct visual inspection. Various non-destructive testing (NDT) techniques have been developed for wire rope inspection, including visual inspection, magnetic flux leakage methods, eddy current testing, and acoustic techniques. These methods are well suited for in-service monitoring of long rope sections; however, their ability to characterize complex internal damage mechanisms and accurately locate defects within the rope structure remains limited [1], [2].

X-ray computed tomography (XCT) has become an established tool for non-destructive evaluation of engineering materials and components, providing volumetric information on internal geometry, manufacturing defects, and damage evolution. This capability makes XCT a promising tool for detailed laboratory investigations and validation of advanced diagnostic methods. The technique has been successfully applied to a wide range of engineering materials, including metallic components, additive-manufactured structures, composite materials, and multi-material systems, where conventional inspection methods often provide only limited access to internal features [3]. Beyond qualitative visualization, XCT enables the quantitative characterization of internal structures through dimensional measurements, defect segmentation, porosity analysis, and crack morphology evaluation, making it a valuable tool for failure analysis, material characterization, model validation, and the development of advanced diagnostic methods [4], [5].

Among the various NDT techniques directly applicable for steel wire rope inspection [6], XCT represents a particularly promising approach due to its ability to provide direct three-dimensional visualization of internal rope architectures, including individual wires, strand geometry, damage morphology, and hidden damage features. However, the application of XCT to steel wire ropes is challenging due to the high X-ray attenuation of steel and the complex geometry of the stranded structures. Reliable detection of fine defects requires high spatial resolution, while sufficient penetration often favors higher-power X-ray sources. Since increased target power is commonly associated with larger focal spot sizes, there is a trade-off between penetration capability and image sharpness, directly affecting damage detectability [7]. Thus, the application of XCT to steel wire ropes and stranded cable systems remains relatively limited. Existing studies have mainly demonstrated the feasibility of visualizing the internal wire arrangement and localized damage features, while the influence of XCT system characteristics and acquisition conditions on damage detectability has not yet been comprehensively investigated, particularly with respect to steel wire rope inspection [8], [9].

In this paper, three laboratory XCT systems with substantially different X-ray imaging chains are compared to assess their capability to detect damage in steel wire ropes. Using intact and damaged rope specimens, as well as an individual fractured steel wire, the study evaluates the influence of source power and focal spot size on image quality, spatial resolution, and damage detectability. The findings contribute to the development of reliable XCT inspection procedures for steel wire rope diagnostics.

2. MATERIALS AND METHODS

2.1. Specimens and damage features

In this study, two types of specimen were investigated, comprising an individual fractured steel wire and steel wire rope segments containing representative damage features. The first specimen consisted of a steel wire segment with a nominal diameter of 5 mm containing a fractured end. The specimen was selected to represent an isolated wire failure and to provide a well-defined fracture feature to evaluate the detectability of fine damage details under different XCT imaging conditions. Additional specimens approximately 100 mm in length were extracted from a 10 mm diameter 6×19 steel wire rope with a polymeric core. The rope consisted of six outer strands surrounding the core, while each strand was composed of individual steel wires with a diameter of approximately 0.65 mm. Both rope specimens were extracted from the same wire rope. One specimen originated from a section without visually identified damage and served as a reference sample. The second specimen was taken from the terminal region of the rope at the fracture location, providing a representative example of a damaged rope segment.

2.2. Experimental setups and imaging procedure

Three in-house developed XCT systems equipped with X-ray sources covering a wide range of target-power levels and focal spot sizes were employed to investigate the capabilities and limitations of laboratory XCT for the non-destructive evaluation of steel wire ropes. All systems were integrated within a common real-time control framework that enabled deterministic synchronization of the X-ray source, detector, and motion-control subsystems, while supporting modular hardware integration and advanced XCT acquisition workflows [10], [11].

Figure 1. Experimental configuration employing a high-power liquid-metal anode X-ray source and a large-area low-noise flat-panel detector.

The first experimental configuration, shown in Figure 1, utilized an in-house developed XCT system equipped with a MetalJet D2+ liquid-metal anode microfocus X-ray source (Excillum AB, Sweden), a CsI flat-panel detector XRD 3025 (Varex Imaging, Germany) with a pixel pitch of 100 µm, and a precision rotary stage carrying an X-ray transparent sample holder. The X-ray source was operated at an acceleration voltage of 160 W and a target power of 250 W with arbitrary focal-spot geometry set to approximately 11 µm × 20 µm. A 2 mm aluminium sheet and a 0.6 mm copper sheet were used for X-ray beam filtering to suppress low-energy components of the emitted spectrum. The reference acquisition protocol consisted of three consecutive full-rotation scans with a defined angular offset, each consisting of 1000 equiangular radiographic projections acquired at a native detector resolution of 3008×2512 pixels. The individual projection sets were subsequently combined to form a reference dataset containing 3000 projections, following a multi-rotation acquisition strategy previously employed for dynamic XCT imaging [12]. Each projection was recorded using 1350 ms integration time. To assess the trade-off between acquisition time and reconstruction quality, additional scans comprising 2000 and 1000 projections were performed on the intact wire rope specimen while keeping all remaining imaging parameters unchanged. The applied imaging geometry resulted in an isotropic voxel size of 16.5 µm, while the total acquisition time of the reference scan was approximately 138 min.

The second experimental configuration, depicted in Figure 2, was based on an XCT system that integrates the sealed-type microfocus X-ray tube L9631 (Hamamatsu Photonics, Japan), the Dexela 1512NDT flat-panel detector (Varex Imaging, Germany) and the precision rotary stage platform ACD 120-80 (Akribis Systems, Singapore) that carried the specimen. The detector features a pixel pitch of 75 µm, an active matrix of 1944×1536 pixels, and 14-bit signal digitization, allowing readout rates of up to 10/s. In contrast to the high-power liquid-metal X-ray source configuration, this setup employed a lower-power microfocus source with a substantially smaller focal spot size. The resulting reduction in focal spot size enabled higher geometric magnification and improved spatial resolution, although at the cost of reduced penetration capability and increased acquisition times. The reference acquisition protocol consisted of 2868 equiangular

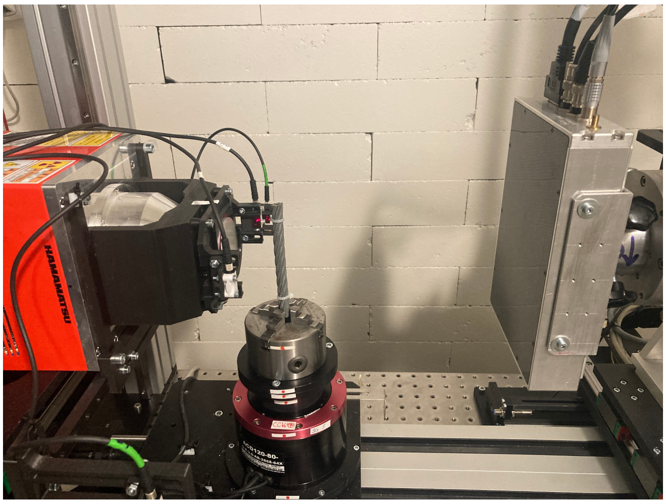

Figure 2. Experimental configuration based on a low-power microfocus X-ray source and a fast flat-panel detector enabling few-micron-resolution XCT imaging.

Figure 3. Experimental configuration employing a high-power X-ray source and a large-area scintillator-coupled detector for large-field-of-view XCT imaging.

radiographic projections acquired at a full detector resolution of 1944 × 1536 pixels. For wire rope specimens, the X-ray tube was operated at an acceleration voltage of 100 kV and a target power of 12 W, resulting in an isotropic voxel size of 16.5 μm. For the fractured steel wire specimen, the source power was reduced to 5 W, allowing an isotropic voxel size of 5.21 μm. To assess the influence of projection count on acquisition time and reconstruction quality, additional datasets comprising 1912 and 956 projections were acquired for the intact wire rope specimen while keeping all remaining imaging parameters unchanged. The practically optimized acquisition strategy based on 1912 projections reduced the acquisition time to approximately 12 min, representing a suitable compromise between image quality and scanning speed for continuous spiral XCT imaging. Following the successful implementation of an in-house spiral XCT acquisition workflow into the Hamamatsu-based XCT system (see [13]), a proof-of-concept spiral acquisition (HRs) was performed using six consecutive revolutions with a spiral pitch of 10 mm. This experiment demonstrates the practical applicability of the optimized acquisition protocol for the continuous laboratory imaging of elongated steel wire rope specimens. The detailed implementation of spiral acquisition, motion synchronization, geometrical compensation, and reconstruction procedures is beyond the scope of the present work and will be reported separately.

The final experimental configuration employed an in-house developed XCT system consisting of a high-power X-ray tube HP-225 (Comet X-ray, Switzerland), a GPXS J10666-311 (Hamamatsu, Japan) large-area CsI scintillating screen, a Kiralux CS135MU optical camera (Thorlabs, USA), and NMV-16 16 mm f/1.4 lens (Navitar, USA). In this case, the specimen was mounted on a servo-driven rotary stage ACD175-A102 (Akribis Systems, Singapore). The experimental setup is shown in Figure 3. The conversion of X-rays to visible light for further detection using a camera was based on a scintillating screen with a CsI conversion layer with a thickness of 400 μm and an active area of 468 mm × 468 mm with a native projection resolution of 1024 × 1024 pixels given by the properties of the camera sensor. Projection pre-processing included dark-field and flat-field corrections, while hot-pixel suppression in the readout of the camera sensor was enabled to deal with zingers in the projections. The X-ray source was operated at an acceleration voltage of 80 kV and a target current of 10 mA, corresponding to a target power of 800 W. The source was configured in small-spot mode with a nominal maximum focal spot size of approximately 400 μm. The reference acquisition protocol consisted of 3647 equiangular radiographic projections with an exposure time of 1800 ms per projection. The total acquisition time was approximately 122 min. The applied imaging geometry resulted in an isotropic voxel size of 112.5 μm.

For clarity, the individual acquisition modes presented throughout the paper are designated according to the employed X-ray source, using the prefixes H (Hamamatsu), M (MetalJet), and C (Comet), while the second letter distinguishes measurements performed on the individual steel wire (W) and the wire rope specimens (R). The designation HRs refers to the proof-of-concept spiral acquisition performed using the Hamamatsu-based setup (see Tables 1 and 2).

All tomographic datasets were reconstructed using cone-beam filtered backprojection based on the modified Feldkamp-Davis-Kress algorithm [14] implemented in VGStudio MAX 2025.1 (Volume Graphics GmbH, Germany). To ensure direct comparability between individual acquisitions, identical reconstruction procedures were applied to all datasets to ensure consistent comparison of image quality and damage detectability between the investigated XCT configurations.

2.3. Image quality evaluation

To enable an objective comparison of the investigated XCT acquisition configurations, the reconstructed image quality was evaluated using two complementary metrics characterizing image contrast and effective spatial resolution. Specifically, the contrast-to-noise ratio (CNR) and the full width at half maximum (FWHM) of the line spread function (LSF) were selected, as they jointly reflect the capability of the imaging system to distinguish fine structural details while preserving edge sharpness. The image quality metrics and their implementation follow the methodology previously reported in [15].

The CNR was determined from the reconstructed tomographic slices by selecting two representative rectangular regions of interest (ROIs) corresponding to homogeneous material and background regions, respectively, as illustrated in Figure 6. The ROIs were manually selected to avoid structural boundaries and other local image artefacts while remaining sufficiently large to provide representative grayscale statistics. The image contrast was defined as the difference between the mean grayscale values of the two regions, while image noise was estimated from the corresponding standard deviations of grayscale intensities. The CNR

Table 1. Summary of the investigated XCT acquisition modes and corresponding imaging parameters, including X-ray source settings, detector configuration, acquisition protocol, and reconstructed voxel size.

Mode	X-ray source	Voltage [kV]	Current [μA]	Filter	N projections	Voxel size [μm]	Detector type	Detector mode
HW1	Hamamatsu	100	50	2 mm Al	1 $\times$ 2868	5.21	Dexela 1512	high well
HW2	Hamamatsu	100	50	2 mm Al	1 $\times$ 2868	5.21	Dexela 1512	high well
HR1	Hamamatsu	100	120	2 mm Al	1 $\times$ 956	16.54	Dexela 1512	high well
HR2	Hamamatsu	100	120	2 mm Al	1 $\times$ 1912	16.54	Dexela 1512	high well
HR3	Hamamatsu	100	120	2 mm Al	1 $\times$ 2868	16.54	Dexela 1512	high well
HR4	Hamamatsu	100	120	2 mm Al + 0.2 mm Cu	1 $\times$ 1912	16.54	Dexela 1512	low well
HR5	Hamamatsu	100	120	2 mm Al + 0.4 mm Cu	1 $\times$ 1912	16.54	Dexela 1512	low well
HR6	Hamamatsu	100	120	2 mm Al	1 $\times$ 2868	16.54	Dexela 1512	high well
HRs	Hamamatsu	100	120	2 mm Al	6 $\times$ 1912	11.22	Dexela 1512	low well
MW1	MetalJet	160	1562	2 mm Al + 0.6 mm Cu	3 $\times$ 1000	16.55	XRD 3025	gain: 3 pF
MR1	MetalJet	160	1562	2 mm Al + 0.6 mm Cu	1 $\times$ 1000	16.55	XRD 3025	gain: 3 pF
MR2	MetalJet	160	1562	2 mm Al + 0.6 mm Cu	2 $\times$ 1000	16.55	XRD 3025	gain: 3 pF
MR3	MetalJet	160	1562	2 mm Al + 0.6 mm Cu	3 $\times$ 1000	16.55	XRD 3025	gain: 3 pF
CR1	Comet	80	10 mA	2 mm Al	1 $\times$ 3647	112.47	scintillator + camera	-

was subsequently calculated as

$$\mathrm{CNR} = \frac{c}{\sqrt{\sigma_1^2 + \sigma_2^2}}, \quad (1)$$

where c denotes the measured image contrast and σ_1 and σ_2 represent the standard deviations of the grayscale values within the individual regions of interest.

The effective spatial resolution was characterized using the FWHM of the LSF. The LSF was obtained from the derivative of the edge spread function (ESF) extracted across a high-contrast material interface [16]. Because direct numerical differentiation substantially amplifies image noise, the measured LSF was approximated by a Gaussian distribution, providing a robust estimate of its characteristic width. Under this assumption, the FWHM can be expressed as

$$\mathrm{FWHM} = 2\sqrt{2\ln(2)}\,\sigma \approx 2.3548\,\sigma, \quad (2)$$

where σ denotes the standard deviation of the fitted Gaussian function. Lower FWHM values correspond to narrower line spread functions and, therefore, indicate improved effective spatial resolution. Together, the CNR and the FWHM provide complementary quantitative descriptors of reconstructed image quality, reflecting both the detectability of low-contrast features and the sharpness of structural boundaries.

In addition to the evaluation of CNR and FWHM characteristics for every considered scanning scenario, flat-field projections (i.e., projections of an open X-ray beam without a specimen) from

Table 2. Quantitative image quality metrics obtained for all investigated XCT acquisition modes, including the contrast-to-noise ratio (CNR), the line spread function full width at half maximum (FWHM), and the corresponding absolute spatial resolution.

Mode	CNR	FWHM [px]	Absolute FWHM [μm]
HW1	8.9	5.80	30.24
HW2	19.1	2.67	13.89
HR1	21.3	3.53	58.94
HR2	24.9	2.83	46.73
HR3	27.8	2.35	38.87
HR4	21.7	4.64	76.79
HR5	14.4	5.42	89.59
HR6	18.9	1.32	21.92
HRs	18.4	16.05	180.05
MW1	23.1	3.69	60.99
MR1	29.2	3.42	56.67
MR2	33.1	3.62	59.85
MR3	38.8	4.42	73.17
CR1	47.1	13.54	1520.31

every imaging chain considered in this study were subjected to intensity distribution analysis to estimate X-ray beam intensity characteristics and response of the utilized radiation imaging detectors. In general, for the considered cone-beam CT (CBCT) procedure, the observed radiation distribution from the cone-beam source is a projection of the X-ray focal-spot such that maximum intensity is obtained on the imaging axis of the chain with a decrease proportional to an angular offset from the imaging axis. However, the resulting projections captured during the imaging procedure are then degraded by random and system errors arising from the type of instrumentation, together with factors such as current state of conversion screen and detector electronics, both affected by radiation damage accumulating over time. Thus, the flat-field projections were calibrated using dark-frame subtraction to remove thermal noise and fixed-pattern defects of the acquisition instrumentation, and the resulting image was fitted by a bi-cubic polynomial surface effectively filtering intrinsic noise present in the projections while obtaining parameters of the fitting expression that can be used to quantify the intensity distribution. The surface fitting procedure was carried out using a third-degree polynomial in x and y denoted by:

$$I\left(x,y\right) = \sum_{i=0}^{n}\sum_{j=0}^{n} p_{\mathrm{i,j}} x^i y^j, \quad (3)$$

where $n = 3$, $\deg I = n$, and $p_{\mathrm{i,j}}$ are coefficients of the polynomial established by fitting the respective flat-field image. As a representative example, Figure 4 shows the intensity plot of I in the calibrated flat-field projection of Comet imaging chain, together with the superimposed polynomial surface derived from the fitting procedure.

3. RESULTS

High-resolution XCT enabled direct three-dimensional visualization of the internal architecture of the investigated steel wire rope specimens. As illustrated in Figure 5, the damaged specimen exhibits a pronounced disruption of the original arrangement of the strands accompanied by multiple fractured and displaced wires, demonstrating the ability of XCT to reveal complex internal damage.

For quantitative comparison of the investigated acquisition modes, the image quality metrics introduced in Section 2.3. were evaluated for all reconstructed datasets. Representative ROIs for material and background, together with the extracted material–background edge profile and the corresponding line spread func-

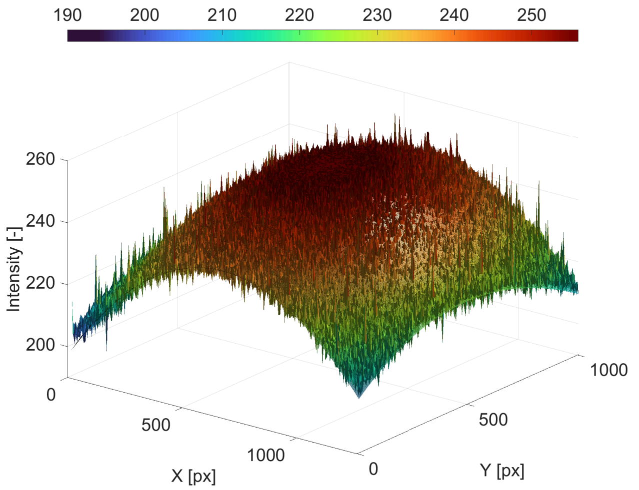

Figure 4. Surface plot of image intensities of the Comet imaging chain, together with the fitted polynomial surface of third-degree.

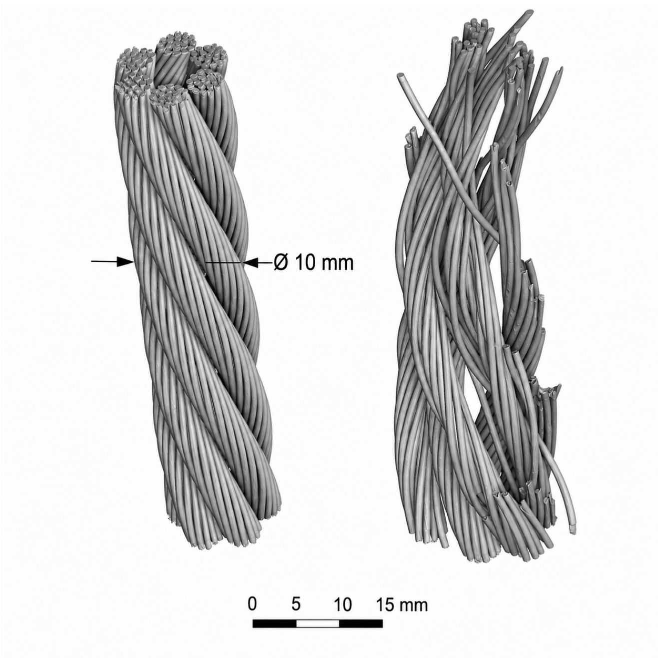

Figure 5. Three-dimensional volume renderings of the intact (left) and damaged (right) steel wire rope specimens reconstructed from the reference XCT acquisition performed using the MetalJet X-ray source and the Varex XRD 3025 detector.

tion, are shown in Figure 6. The resulting CNR and FWHM values are summarized in Table 2.

A particularly informative comparison is provided by the HR1, HR2, and HR3 datasets, which were acquired using identical imaging geometry, while differing only in the number of acquired projections. With increasing projection count, the CNR increased from 21.3 to 27.8, indicating reduced reconstruction noise due to more complete angular sampling. Simultaneously, the FWHM decreased from 3.53 to 2.35 pixel, corresponding to a sharper material–background transition and improved effective spatial resolution. This trend demonstrates that, for the Hamamatsu-based configuration, increasing the number of projections improves both image contrast and edge definition, although at the expense of longer acquisition time.

A different behaviour was observed for the MR1, MR2, and

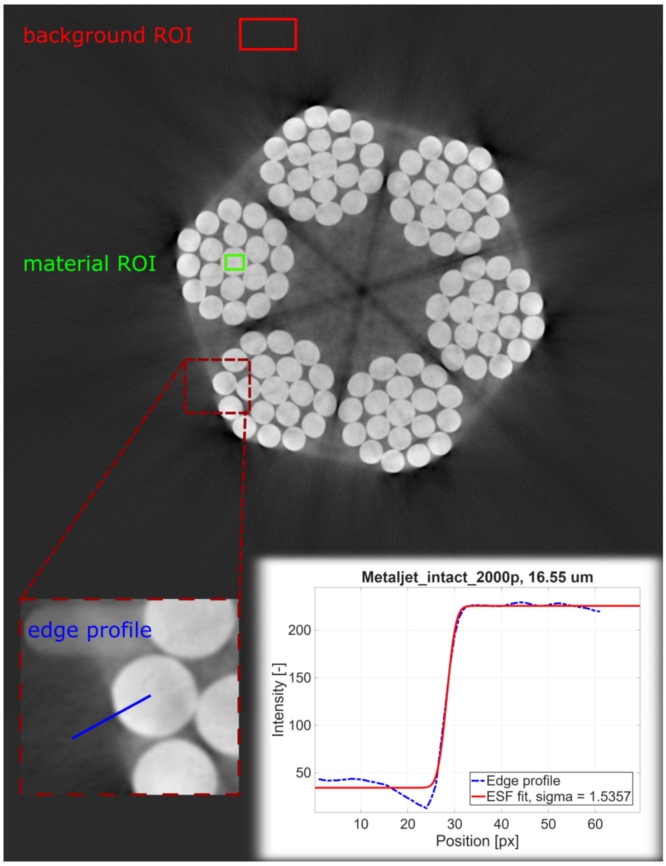

Figure 6. Representative transversal section of the tomographic reconstruction of the rope acquired using the MetalJet X-ray source with 2×1000 projections (measurement mode MR2), showing the selected material–background interface used for edge profile extraction and subsequent line spread function (LSF) evaluation.

MR3 datasets, which were acquired using the MetalJet configuration under identical imaging geometry but with an increasing number of accumulated projection sets. In this case, the CNR increased consistently from 29.2 to 38.8, confirming the expected reduction in image noise. However, FWHM also increased from 3.42 to 4.42 pixel, indicating a slight degradation of edge sharpness despite the improved noise characteristics. This suggests that for this acquisition mode, improved signal statistics were accompanied by a modest loss of effective sharpness, most likely related to the longer effective acquisition procedure and the accumulation of small system instabilities during repeated projection acquisition.

The additional datasets provide complementary information on the influence of selected acquisition parameters and imaging configurations. The HR4 and HR5 datasets demonstrate the effect of additional beam filtration, while HR6 represents an acquisition protocol optimized for spatial resolution. The HRs dataset confirms the feasibility of the proposed spiral acquisition approach for damage visualization. The HW1, HW2, and MW1 datasets further demonstrate that the observed image quality trends remain applicable to fractured single-wire specimens, whereas the CR1 dataset illustrates the performance achievable with the high-power Comet configuration. Although these datasets were acquired under different experimental conditions and are therefore not directly comparable in a strictly quantitative manner, they consistently support the overall conclusions regarding the influence of acquisition parameters on image quality and the practical applicability of the investigated laboratory XCT systems.

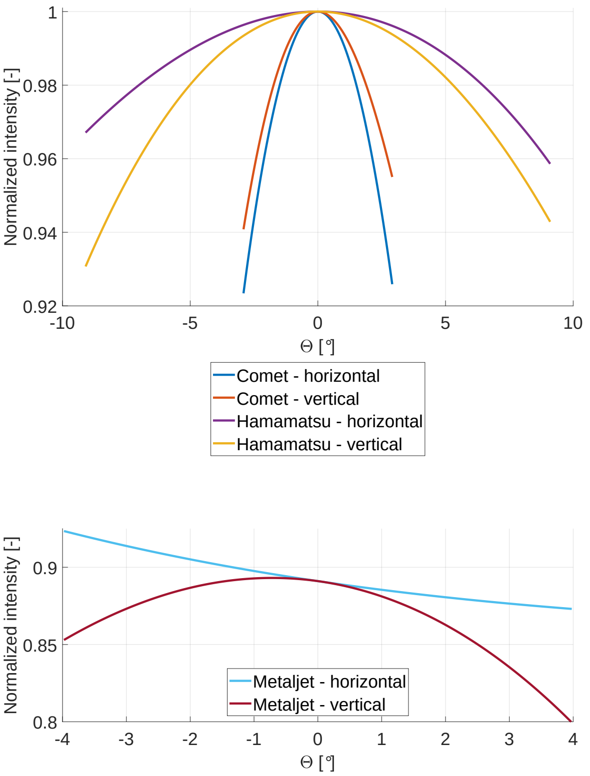

Figure 7. Normalized intensity distributions in vertical and horizontal direction with respect to angle Θ from optical axis of all the used imaging chains.

In the analysis of intensity distribution from the flat-field projections fitted by polynomial surfaces, it is possible to study the response of the imaging chain with respect to angular offset from its optical axis. Here, vertical and horizontal profiles intercepting the optical axis were used, the resulting intensity was normalized with respect to the maximum in the respective projection, and the plots were centered around the optical axis of the imaging chains. The plot for all imaging chains is shown in Figure 7.

The plots of image intensity with respect to angle Θ then show typical properties of all the used X-ray radiation imaging chains. In the case of the Comet scanner equipped with a high-power X-ray source, a large-area scintillating screen, and a laboratory high-speed camera, a rapid decrease of approximately 4 % to 8 % within only 3 degrees of cone beam divergence can be observed. This effect results from the combined influence of the decreasing X-ray beam intensity and the optical properties of the large field-of-view imaging lens attached to the laboratory camera. In contrast, the imaging chain based on the Hamamatsu microfocus source coupled with CsI-based CMOS detector leads to a comparable absolute image intensity decrease, but on a three-fold larger angular section. However, the most significant difference can be seen in the case of the MetalJet source and the Varex large area flat-panel detector, where the horizontal intensity distribution is composed of multiple increases and decreases forming a column-like pattern resulting from the non-uniform response of the detector. The acquired results for all imaging chains highlight the need for X-ray projection calibration with at least flat-field correction before the CT reconstruction procedure, and also help to explain possible differences in imaging quality of, e.g., the internal and external surfaces of the steel wire ropes.

The practically optimized acquisition protocol identified in the present study enabled the successful implementation of a proof-of-concept of continuous spiral XCT imaging of elongated steel wire rope specimens, demonstrating a feasible pathway towards inspection of longer components [13]. Future improvements in inspection efficiency are expected from dedicated XCT inspection systems that combine continuous spiral acquisition with high-speed photon-counting detectors and modern real-time acquisition and control electronics [17].

4. CONCLUSIONS

The present study demonstrates the applicability of laboratory X-ray computed tomography for non-destructive visualization of the internal structure of steel wire ropes. The comparison of three complementary XCT configurations confirmed that appropriate selection of the imaging system and acquisition parameters enables reliable visualization of individual wires, strand arrangement, and representative internal damage features. The results further highlight the importance of balancing spatial resolution, penetration capability, image quality, and acquisition time for reliable laboratory inspection of steel wire rope specimens.

Although high-resolution laboratory XCT remains prohibitively time-consuming for routine inspection of extended steel wire rope sections, the presented results demonstrate that the method is well suited to a detailed examination of short damaged rope segments under laboratory conditions. Its ability to provide direct three-dimensional visualization of the internal rope architecture makes XCT a valuable complementary tool for detailed structural characterization, localized damage assessment, and development and validation of advanced non-destructive testing methods.

The comparison demonstrated that none of the investigated XCT configurations simultaneously satisfies all the requirements for the high-resolution inspection of steel wire ropes. Each system exhibited specific advantages together with inherent limitations, reflecting the trade-off between penetration capability, spatial resolution, image quality, and acquisition time. Consequently, the selection of an appropriate XCT configuration should be guided by the specific inspection objective rather than the characteristics of the individual system alone.

AUTHORS' CONTRIBUTION

Daniel Kytyr: Conceptualization, Methodology, Investigation, Software, Formal analysis, Writing – original draft, Visualization. **Petr Koudelka**: Investigation, Software, Validation, Writing – Review & editing. **Jan Sleichrt**: Investigation, Software, Validation, Writing – review & editing. **Jaroslav Kylar**: Resources, Investigation, Writing – review & editing. **Radka Hrazdirova**: Resources, Investigation, Writing – review & editing. **Jiri Lahodny**: Supervision, Resources, Conceptualization, Funding acquisition.

DATA AVAILABILITY STATEMENT

Representative experimental data supporting this study are publicly available in the Zenodo repository DOI: 10.5281/zenodo.21100938.

ACKNOWLEDGMENT

The research was supported by the European Union under the INODIN project no. CZ.02.01.01/00/23_020/0008487.

REFERENCES

[1] S. Liu, Y. Sun, X. Jiang, Y. Kang, A review of wire rope detection methods, sensors and signal processing techniques, Journal of Nondestructive Evaluation, vol. 39, 2020, no. 4. DOI: 10.1007/s10921-020-00732-y

[2] P. Zhou, G. Zhou, Z. Zhu, Z. He, X. Ding, C. Tang, A review of non-destructive damage detection methods for steel wire ropes, Applied Sciences, vol. 9, 2019, no. 13, p. 2771. DOI: 10.3390/app9132771

[3] A. du Plessis, S. G. le Roux, A. Guelpa, The CT scanner facility at stellenbosch university: An open access X-ray computed tomography laboratory, Nuclear Instruments and Methods in Physics Research Section B: Beam Interactions with Materials and Atoms, vol. 384, 2016, p. 42–49. DOI: 10.1016/j.nimb.2016.08.005

[4] E. Maire, P. J. Withers, Quantitative X-ray tomography, International Materials Reviews, vol. 59, 2014, no. 1, p. 1–43. DOI: 10.1179/1743280413y.0000000023

[5] H. Villarraga-Gómez, E. L. Herazo, S. T. Smith, X-ray computed tomography: from medical imaging to dimensional metrology, Precision Engineering, vol. 60, 2019, p. 544–569. DOI: 10.1016/j.precisioneng.2019.06.007

[6] P. Mazurek, A comprehensive review of steel wire rope degradation mechanisms and recent damage detection methods, Sustainability, vol. 15, 2023, no. 6, p. 5441. DOI: 10.3390/su15065441

[7] J. Rueckel, M. Stockmar, F. Pfeiffer, J. Herzen, Spatial resolution characterization of a X-ray microCT system, Applied Radiation and Isotopes, vol. 94, 2014, p. 230–234. DOI: 10.1016/j.apradiso.2014.08.014

[8] K. Kishore, G. Mukhopadhyay, Novel degradation mechanism of a structural wire rope during its life cycle, Metallography, Microstructure, and Analysis, vol. 8, 2019, no. 2, p. 189–200. DOI: 10.1007/s13632-018-0511-9

[9] H. Huang, H. Tian, X. Cui, X. Xu, Adaptive wire rope breakage detection in CT images based on template matching and optimization, Russian Journal of Nondestructive Testing, vol. 61, 2025, no. 10, p. 1211–1221. DOI: 10.1134/s1061830925604647

[10] D. Kytýř, L. Zárybnická, V. Rada, P. Zlámal, P. Koudelka, J. Machotová, J. Šleichrt, R. Ševčík, Full-field deformation characteristics of preserved sandstone via automated 4D X-ray CT procedure, Measurement, vol. 258, 2026, p. 119495. DOI: 10.1016/j.measurement.2025.119495

[11] D. Vavřík, T. Fíla, P. Koudelka, D. Kytýř, M. Macháček, V. Rada, J. Valach, P. Zlámal, Phase-locked X-ray computed tomography for modal analysis of periodically oscillating structures, Measurement, vol. 258, 2026, p. 119395. DOI: 10.1016/j.measurement.2025.119395

[12] M. Jadidi, M. Båth, S. Nyrén, Dependency of image quality on acquisition protocol and image processing in chest tomosynthesis—a visual grading study based on clinical data, The British Journal of Radiology, 2018, p. 20170683. DOI: 10.1259/bjr.20170683

[13] V. Rada, D. Vavrik, J. Kunecky, D. Kytyr, Spiral X-ray computed tomography of long wooden samples: Influence of pitch and geometric calibration on reconstruction quality, Acta IMEKO, vol. 15, 2026, no. 3, pp. 1–6. DOI: 10.21014/actaimeko.v15i3.2456

[14] L. A. Feldkamp, L. C. Davis, J. W. Kress, Practical cone-beam algorithm, Journal of the Optical Society of America A, vol. 1, 1984, no. 6, p. 612. DOI: 10.1364/josaa.1.000612

[15] M. Vopalensky, P. Koudelka, J. Sleichrt, I. Kumpova, M. Borovinsek, M. Vesenjak, D. Kytyr, Fast 4D on-the-fly tomography for observation of advanced pore morphology (APM) foam elements subjected to compressive loading, Materials, vol. 14, 2021, no. 23, p. 7256. DOI: 10.3390/ma14237256

[16] G. C. Holst, Testing and Evaluation of Infrared Imaging Systems, Third Edition, SPIE, 2008, ISBN: 9780819472472. DOI: 10.1117/3.2588946

[17] P. Burian, P. Broulím, B. Bergmann, M. Farkaš, M. Jára, O. Růžička, P. Smolyanskiy, P. Mánek, Katherine generation 2: Advanced readout system for Timepix3 detectors, Journal of Instrumentation, vol. 20, 2025, no. 06, p. C06077. DOI: 10.1088/1748-0221/20/06/c06077